

# A Microelectromechanical System for Nano-Scale Testing of One Dimensional Nanostructures

B. Peng<sup>1</sup>, Y. Zhu<sup>1</sup>, I. Petrov<sup>2</sup>, and H. D. Espinosa<sup>1,\*</sup>

<sup>1</sup>Northwestern University, Mechanical Engineering, 2145 Sheridan Rd., Evanston, IL 60208-3111, USA

<sup>2</sup>University of Illinois, Frederick Seitz Materials Research Laboratory, 104 S. Goodwin Av., Urbana, IL 61801, USA

(Received: xx Xxxx xxxx. Revised/Accepted: xx Xxxx xxxx)

*In situ* electron microscopy tensile tests of nanowires and carbon nanotubes performed using a MEMS-based material testing system are reported. The development of the material testing system (previously reported elsewhere<sup>23–26</sup>) is briefly reviewed. This system, consisting of a surface micromachined actuator and load sensor, makes possible continuous observation of specimen deformation and failure with sub-nanometer resolution, while simultaneously measuring the applied load electronically with nanonewton resolution. This letter begins with a brief review of some of the methods used in mechanical characterization of nanoscale specimens, followed by a description of the MEMS-based material testing system. Finally, emphasis is placed on experimental results demonstrating the advantages of the MEMS-based system.

**Keywords:** Material Testing, Carbon Nanotube, Nanowire.

## 1. INTRODUCTION

Methods for nanomechanical characterization of materials have recently attracted significant attention due to the emergence of various novel nano-scale materials and structures in the past decade. For example, nanotubes and nanowires are seen as ideal structures for use in a variety of applications ranging from nanocomposites to nano-electromechanical systems. However, their scale presents a new set of challenges to the mechanics community. Identification of their properties and deformation mechanisms requires techniques of loading, measuring, and imaging with finer resolutions than previously achieved. As a result, these structures demand quantitative *in situ* mechanical testing in scanning or transmission electron microscopes (SEM or TEM), or scanning probe microscopes (SPM).

The Young's modulus of nanostructures can be estimated by observing their vibrations. Treacy et al.<sup>1</sup> determined the Young's modulus of multi-walled carbon nanotubes (MWNTs) by measuring the amplitude of their thermal vibrations within a TEM. The Young's modulus of the MWNT was estimated based on the size of the envelope of the vibration. Poncharal et al.<sup>2</sup> measured the Young's modulus of MWNTs by inducing resonance within a TEM. By increasing the driving frequency to the

point of resonance, the authors were able to estimate the Young's modulus based on the measured geometry of the MWNTs and their resonance frequency. These techniques do not provide a true measurement of load or deformation and do not allow for imaging of the specimen as the vibration is significantly faster than the scan speed of the imaging beam.

Bending techniques, including force spectroscopy atomic force microscopy (AFM),<sup>3</sup> nanoindentation,<sup>4</sup> and on-chip testing,<sup>5,6</sup> involve application of a known bending force while measuring the resulting displacement. Wong et al.<sup>7</sup> measured the Young's modulus, strength, and toughness of MWNTs and SiC nanorods using an atomic force microscope (AFM). The nanostructures were randomly dispersed on a flat substrate and pinned in place by micro-fabricated patches. The AFM was then used to bend the cantilevered structures transversely. By measuring the lateral force applied to the AFM probe by the nanostructure, the authors were able to obtain force versus deflection data at various locations along the length of the structure. To avoid adhesion, Walters et al.<sup>8</sup> suspended MWNTs over a microfabricated trench before bending them laterally with an AFM. Salvétat et al.<sup>9</sup> dispersed MWNTs over an alumina ultrafiltration membrane with 200 nm pores. This created similarly suspended nanostructures. The authors then deflected the suspended MWNTs vertically using an AFM probe in contact mode to obtain

\*Corresponding author; E-mail: espinosa@northwestern.edu

similar force-displacement measurements. Again, these techniques typically lack the ability to image the specimen during loading.

The tensile test is perhaps the most direct method of determining the Young's modulus of a material. Some tensile techniques allow for simultaneous load measurement and local imaging by AFM,<sup>10</sup> optical interferometry,<sup>11</sup> or scanning electron microscopy (SEM).<sup>12,13</sup> On a larger scale, Pan et al.<sup>14</sup> used a stress-strain rig to load a long (approximately 2 mm) MWNT rope in tension. This rope contained tens of thousands of parallel nanotubes. Sharpe et al.<sup>11</sup> loaded thin films in tension while simultaneously measuring displacement using either a capacitance-based displacement probe or laser interferometry, depending on the size of the sample. These techniques tend to be better suited to the micrometer scale and not to the study of nanostructures such as nanotubes or nanowires due to their limited resolution. Likewise, Espinosa et al.<sup>15–18</sup> investigated size scale plasticity, strength and fracture toughness of freestanding thin film materials using a nanoindenter as a loading device.

On a smaller scale, Yu et al.<sup>12</sup> and Ding et al.<sup>13</sup> used a micro- or nanomanipulator to conduct *in situ* SEM tensile testing of MWNTs. Likewise, Marszalek et al.<sup>3</sup> attached a gold nanowire to an AFM probe of known stiffness. By lifting the probe a prescribed amount using the piezoelectric actuators of the AFM and observing the corresponding deflection of the probe, they were able to deduce the force applied to the nanowire and corresponding displacement.

Other techniques combine microfabricated and larger-scale devices. These allow alternating SEM or TEM imaging and load or deformation measurement modes through switching of the imaging electron beam between the specimen and microfabricated beams used as load sensors.<sup>19,20</sup> During this switching, important local deformation events may go unobserved. Finally, some techniques have been developed to provide real time images of the specimen during loading. However, quantitative measurement of load and deformation are not provided independently.<sup>21,22</sup>

The methods described above represent some of the significant progress made recently in the mechanical testing of nanostructures. However, lack of control in experimental conditions or limited accuracy of force and displacement measurements can limit their applicability. Recent advances in microelectromechanical systems (MEMS) create the potential for material testing systems that overcome some of the described limitations. MEMS lend themselves naturally to material testing at the nanometer scale. These systems consist of combinations of micromachined elements, including strain sensors and actuators, integrated on a single chip. Due to their intermediate size, MEMS serve as an excellent interface between the macro and nano world. Their extremely fine force and displacement resolution allows accurate measurement and transduction of forces and displacements relevant at the nanometer scale.

## 2. METHODOLOGY

The MEMS-based material testing system described here has previously been reported in detail.<sup>23–26</sup> For the purposes of this article, we briefly review the device so that the following experimental results and the way in which they were obtained may be more clearly understood. The device consists of three parts: an actuator, a load sensor, and a gap between them for placement of nanostructures, as shown in Figures 1(a) and (b). The devices were fabricated at MEMSCAP (Durham, NC) using the Multi User MEMS Process (MUMPs). Two types of actuators, an electrostatic (comb-drive) actuator<sup>27–29</sup> and an electrothermal actuator<sup>30,31</sup> were used to apply time-dependent forces or displacements, respectively. The load sensor operates on the basis of differential capacitive sensing.<sup>23–25</sup> The sensor displacement is determined by the measured capacitance change. This displacement is used to compute the applied force based on the known stiffness of the sensor. The design of the actuator and load sensor will be described later.

Figure 1(a) shows the entire device. The electrothermal actuator acts as a “displacement control” in the sense that it applies a prescribed displacement to the specimen regardless of the force required to achieve this displacement (within the functional range of the device). The load sensor is suspended on a set of folded beams of known

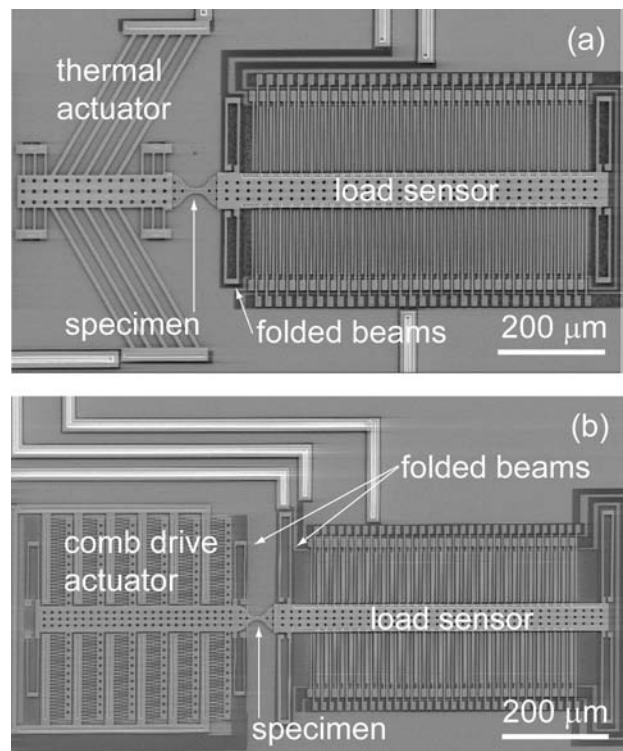


**Fig. 1.** Two variations of the MEMS-based material testing stage. (a) “Displacement controlled” device using a thermal actuator and differential capacitive load sensor. (b) “Force controlled” device using an electrostatic comb-drive actuator and differential capacitive load sensor.

stiffness and measures the corresponding tensile force applied to the specimen. Figure 1(b) shows an alternative loading stage using an electrostatic rather than a thermal actuator. The electrostatic actuator works as a “force control,” applying a prescribed force regardless of the resulting displacement (again within a functional range).

The thermal actuator has the capability of testing stiff structures, e.g., nanoscale thin films and large diameter NWs, while the comb drive actuator is better-suited for relatively compliant structures, which deformation is force controlled. While both the thermal and electrostatic actuators lend themselves nicely to standard microfabrication techniques, the remainder of this letter focuses on the device using the thermal actuator as a case study in the design and modeling involved in building such a device. Electrostatic actuators have been thoroughly described elsewhere, for example.<sup>5,32,33</sup>

In our design for *in situ* SEM testing, 20 devices with different types of actuators and load sensors are arranged on a  $10 \times 10 \text{ mm}^2$  chip. To make electrical connection, there are 100 gold pads fabricated around the periphery of the chip. The chip is glued to the cavity of a ceramic pin grid array package, and the gold pads are wire-bonded to the 100 leads around the cavity as shown in Figure 2(a). The corresponding pins in the back of the package make the electric connection to a printed circuit board, which in turn is connected to electronic actuation and measuring instrumentation.

Measuring capacitance changes with subfemtofarad resolution, as required in this application, is quite challenging. Fortunately, a method to measure charge that mitigates the effect of parasitic capacitance has been developed by the MEMS community.<sup>34,35</sup> A commercially available integrated circuit based on this method, Universal Capacitive Readout MS3110 (MicroSensors, Costa Mesa, CA), is used here. The MEMS device chip is positioned close to the integrated sensing chip on the circuit board to minimize amplified electromagnetic interference (Fig. 2(a)). The output voltage is proportional to the capacitance change.

In addition to the *in situ* SEM measurements reported here, this device has the potential to impact other nanoscale characterization techniques. For instance, *in situ* TEM testing of nanostructures is possible with the addition of a microfabricated window beneath specimen gap to allow the imaging beam to pass through the device substrate. The major challenge here is to etch the window, from the back of the silicon wafer, without damaging the previously fabricated structures. We accomplished this task by deep reactive ion etching of the window before releasing the devices.<sup>23,26</sup> Figure 2(b) shows a MEMS chip ( $5 \times 10 \text{ mm}$ ) containing four MEMS devices. The two devices in the center are used for *in situ* TEM testing, while the other two devices are used in calibration tests. The chip has eight contact pads for electric actuation/sensing. The chip is designed to be directly mounted on a specially designed

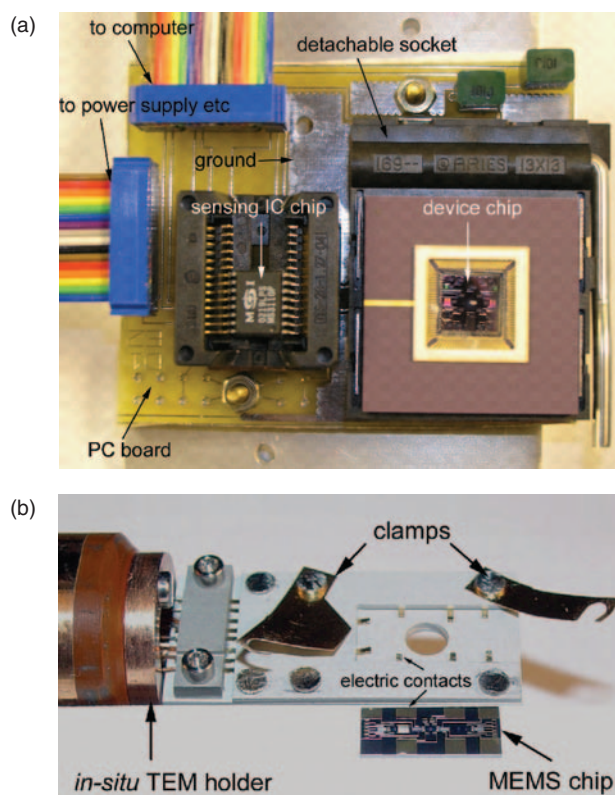


**Fig. 2.** (a) Experimental setup for *in situ* SEM testing. The MEMS device chip is positioned near the MS3110 chip on a printed circuit board. The setup is connected to a power supply, a digital multimeter, and a computer outside the SEM by means of a chamber feedthrough. (b) *In situ* TEM holder (containing a feedthrough and eight electric contact pads)<sup>36</sup> along with a  $5 \times 10 \text{ mm}$  MEMS chip. In an actual experiment, the MEMS chip is flipped, placed in the TEM holder, and fixed by the left and right clamps.

TEM holder containing a feed-through and interconnects to electrically address the devices (Fig. 2(b)).<sup>23,36</sup> In this case, the sensing integrated circuit chip (MS3110) used in the capacitance measurement is located outside of the TEM.

## 2.1. Electrothermal Actuator Design

Electrothermal actuation complements electrostatic schemes as a compact, stable, high-force actuation technique.<sup>37</sup> Various forms of thermal actuators have been employed in systems ranging from linear and rotary microengines,<sup>38</sup> to two-dimensional nano-scale positioners,<sup>39</sup> optical benches,<sup>40</sup> and instrumentation for material characterization.<sup>41</sup> By incorporating compliant mechanisms larger displacements can be achieved.<sup>39</sup>

Modeling of the thermal actuators generally takes one of two approaches:

- (1) A sequential electro-thermal and thermo-structural analysis<sup>42–44</sup> or;
- (2) A complete coupled three-dimensional finite element analysis (FEA).<sup>45</sup>

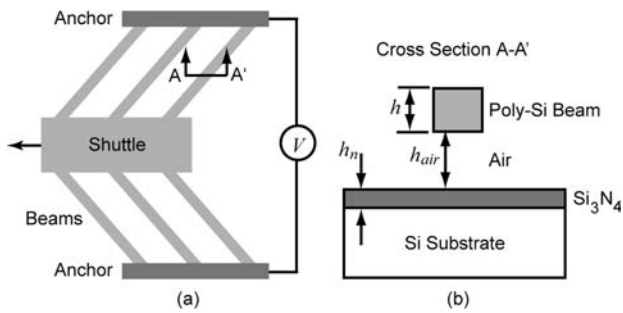


Fig. 3. (a) Schematic of the thermal actuator. (b) Cross section of a single beam suspended over the substrate.

Additional analyses include characterization of the temperature-dependent electro-thermal properties<sup>37,45</sup> of these devices. A schematic of the thermal actuator to be analyzed is shown in Figure 3. The thermal actuator consists of a series of inclined polysilicon beams supporting a free-standing shuttle. One end of each of the inclined beams is anchored to the substrate while the opposite end connects to the shuttle. Thermal expansion of the inclined beams, induced by Joule heating, causes the shuttle to move forward. This heating is the result of current flowing through the beams driven by a voltage applied across the two anchor points.<sup>46</sup> Modeling of these actuators requires a two-step analysis; first an electrothermal analysis to determine the temperature distribution in the device, followed by a thermostructural analysis to determine the resulting displacement field.

An electrothermal model of the device is developed to determine the temperature distribution as a function of the applied voltage. This is highly dependent upon the operating environment. When operating in air, the dominant heat transfer mechanism is heat conduction between the actuator and substrate through the air-filled gap between them.<sup>43,44,46</sup> Here the governing equation is,

$$k_p \frac{d^2 T}{dx^2} + J^2 \rho = \frac{S}{h} \frac{T - T_s}{R_T} \quad (1)$$

where  $k_p$  and  $\rho$  are the thermal conductivity and resistivity respectively of the polysilicon beams;  $J$  is the current density;  $S = h/w(2h_{air}/h + 1) + 1$  is a shape factor accounting for the effect of element shape on heat conduction to the substrate;  $R_T = h_{air}/k_{air} + h_n/k_n + h_s/k_s$  is the thermal resistance between the polysilicon beam and substrate;  $h$  and  $w$  are the thickness and width of a single beam respectively;  $h_{air}$  is the gap between the beam and silicon nitride layer on the substrate;  $h_n$  is the thickness of the silicon nitride;  $h_s$  is the representative thickness of the substrate;  $k_{air}$ ,  $k_n$ ,  $k_s$  are the thermal conductivities of air, silicon nitride, and the substrate respectively; and  $T_s$  is the temperature of the substrate.

The thermal conductivities  $k_p$  and  $k_{air}$  are both temperature dependent. However, the assumption of a constant  $k_p$  yields results similar to those using a

temperature-dependent value of  $k_p$ .<sup>42</sup> Assuming a constant  $k_p$  and temperature dependent  $k_{air}$ , the finite difference method is implemented to solve (Eq. (1)) by writing the second-order differential equation in the form  $d^2 T/dx^2 = b(x, T)$ , and approximating it as,

$$\frac{d^2 T}{dx^2} \approx \frac{1}{(\Delta x)^2} (T_{i+1} - 2T_i + T_{i-1}) \quad (2)$$

Figure 4(a) shows the steady-state temperature profile obtained for a two-leg (one pair of inclined beams) thermal actuator operating in air. The temperature of the shuttle is significantly lower than that of the majority of each beam. This is due to the relatively low current density in the shuttle, resulting in a lower rate of heat generation as compared to that of the beams. Furthermore the relatively large area of the shuttle results in greater heat dissipation through the air to the substrate.

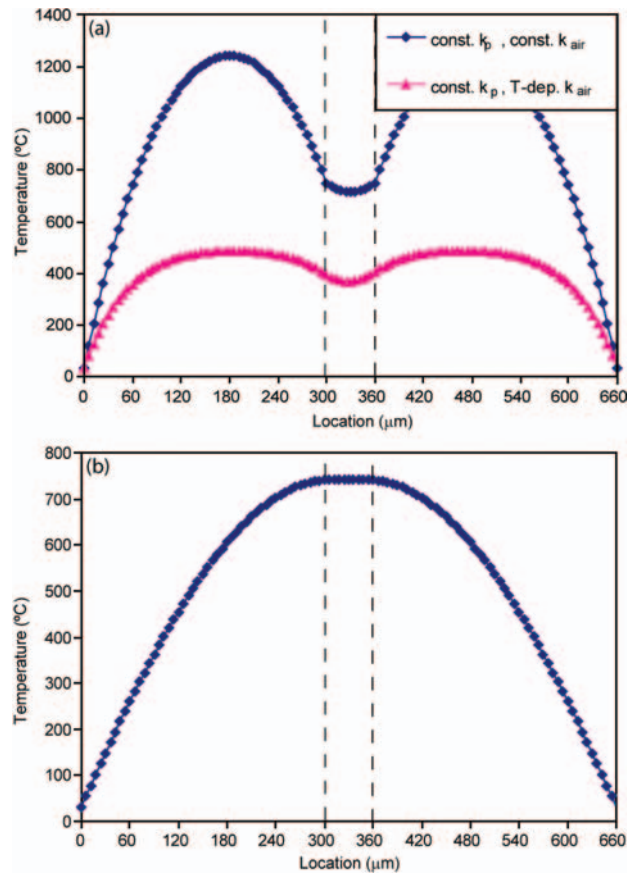


Fig. 4. Steady state temperature profile (with respect to the substrate) along a pair of inclined beams and the shuttle while operated (a) in air for both constant and temperature-dependent values of  $k_{air}$ , and; (b) in vacuum with an input current of 10 mA. In both cases, locations 0–300  $\mu\text{m}$  and 360–660  $\mu\text{m}$  correspond to the thermal beams while the center region is the shuttle between the beams. The beams are anchored to the substrate at 0 and 660  $\mu\text{m}$ . In air, the highest temperature occurs in the beams. In vacuum, the temperature depends most upon the distance from the anchor points (which are now assumed to be the only source of heat dissipation) and thus the shuttle reaches the highest temperature.

The thermal conductivity of the air has a significant effect on the actuator behavior.<sup>43</sup> This strong dependence is clearly seen in Figure 4(a), where the only difference between the two curves is the temperature dependence of the thermal conductivity of air.  $k_{\text{air}}$  increases with temperature, increasing the heat flow between the beams and shuttle and the substrate. Consequently the temperature of the beams and shuttle is lower for a given current flow. Clearly decreasing heat conduction through the air increases the temperature of the beams. Ultimately, operation in vacuum maximizes the beam temperature for a given current flow, making the device more efficient.

In contrast, heat dissipation by conduction through the anchors to the substrate dominates in vacuum.<sup>43, 46</sup> Assuming each beam is thermally independent, an electrothermal model based on a single beam is presented.<sup>43</sup> Heat transfer within the beam is treated as a one-dimensional problem since the length dimension is significantly larger than either of the cross-sectional dimensions. To analyze the case where the thermal actuator operates in vacuum, the term for heat conduction through the air is removed from (Eq. (1)),

$$k_p \frac{d^2 T}{dx^2} + J^2 \rho = 0 \quad (3)$$

Figure 4(b) shows that the highest temperature now occurs in the shuttle rather than in the beams. Here the temperature depends most upon the distance from the anchor points which are now assumed to be the only source of heat dissipation. Since the shuttle is furthest from the anchors, it reaches the highest temperature. With the temperature distribution now known from the electrothermal analysis, the thermomechanical behavior of the actuator is modeled to determine the resulting displacement (see Refs. [24–26]).

While the displacement of the actuator in vacuum is easily characterized experimentally,<sup>24</sup> the temperature distribution is more difficult to obtain. Therefore a coupled-field simulation is particularly necessary. This analysis also helps to assess the temperature at the actuator-specimen interface and to examine the effectiveness of the thin heat sink beams in controlling the temperature increase of the specimen during actuation.<sup>26</sup>

The MEMS-based tensile stage is intended to operate within the SEM or TEM. Thus the following finite element

electrothermal analysis is carried out for the case where the device operates in vacuum. The actuation voltage applied across the anchor points serves as the input while the output includes both the actuator temperature and displacement fields. Displacements at the anchor points are held fixed in the mechanical boundary conditions. The thermal boundary conditions dictate a constant temperature at the anchors.

Figures 5(a, b) depicts the temperature and displacement in the thermal actuator for an actuation voltage of 1 V. As previously described, heat dissipation through the anchors is the dominant dissipation mechanism. Since the shuttle is furthest from the anchors, the highest temperature occurs in the shuttle. Due to the non-uniformity of the temperature distribution, the displacement is also non-uniform.

Heating of the specimen during actuation is unavoidable as a result of the increased temperature of the shuttle to which the sample is attached. However, this effect is minimized with the addition of a series of heat sink beams running between the shuttle and substrate near the shuttle-specimen interface as shown in Figures 5(c, d). To avoid out-of-plane bending another three pairs of heat sink beams are placed at the opposite end of the shuttle. Comparing this to the case without the heat sink beams (Figs. 5(a, b)) this configuration allows for more than twice the displacement at the specimen end of the shuttle for the same allowable temperature increase at the shuttle-specimen interface. The problem of specimen heating can be further mitigated with the addition of a thermal isolation layer between the actuator and specimen following the custom microfabrication process<sup>46</sup> for highly temperature-sensitive samples.

The thermal actuator is calibrated experimentally to verify the analytical and FEA models described above. Figure 6<sup>24</sup> shows a comparison of the analytical and FEA predictions of actuator displacement for a given current input with experimentally-measured results. The displacement of the actuators was measured in the SEM,<sup>25</sup> giving spatial resolution of better than 5 nm. Using the analytical model, the displacement is computed based on experimentally-measured temperatures in the actuator.<sup>24</sup> In order to obtain the resulting current, the resistance of the actuator is computed using the output temperature and a

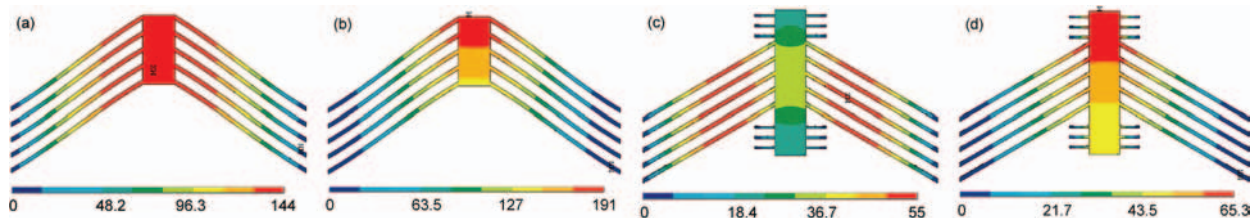


**Fig. 5.** (a) Temperature increase (°C) and (b) displacement field (nm) in the thermal actuator. The displacement component plotted is in the shuttle axial direction. (c) Temperature (°C) and (d) displacement field (nm) in the thermal actuator with three pairs of heat sink beams at the specimen end. In this analysis, the heat sink beams are 40  $\mu\text{m}$  in length and 4  $\mu\text{m}$  wide with 16  $\mu\text{m}$  spacing between them. ANSYS Multiphysics, version 6.1 was used in this analysis.

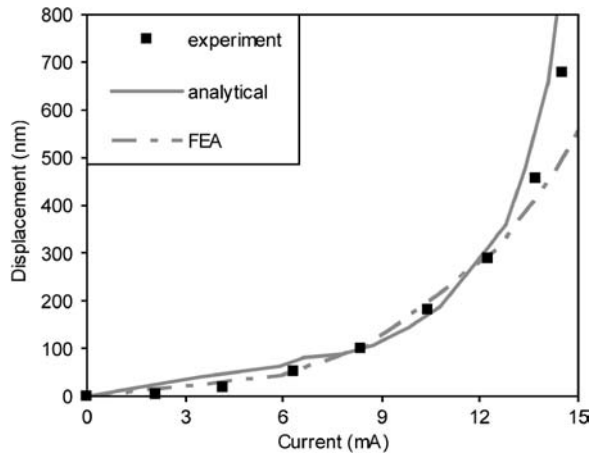


**Fig. 6.** Comparison of displacement at the actuator-specimen interface as predicted by the analytical and FEA models and measured experimentally. Displacement is plotted as a function of the input current.

value of resistivity corresponding to the average temperature of the device.<sup>24</sup>

The models agree well with the experimentally-measured actuator displacements as shown in Figure 6. This suggests the models are useful in predicting the behavior of thermal actuators of other geometry. At large currents (above approximately 12 mA), both the analytical and FEA models deviate slightly from the experimental results. This can be explained largely by inaccuracies in material parameters such as resistivity and thermal conductivity at high temperatures.<sup>37,43</sup> Furthermore, the microstructure of polysilicon begins to be modified at these high current levels and elevated temperatures.<sup>24</sup>

## 2.2. Load Sensor Design

The load sensor consists of a differential capacitive displacement sensor suspended on a set of elastic members of known stiffness. By calibrating the stiffness of the sensor,<sup>25,26</sup> the load is computed based on the measured displacement. The differential capacitive displacement sensor<sup>34,35,47</sup> is chosen for its sensitivity and linear behavior over a range of displacements appropriate for tensile testing of nanostructures.

The differential capacitive sensor is comprised of a movable rigid shuttle with electrodes (or “fingers”) pointing outward as shown schematically in Figure 7(a).<sup>25</sup> These fingers are interdigitated between pairs of stationary fingers (Fig. 7(b)) fixed to the substrate. Under no load each movable finger sits centered between the two stationary fingers. Each set of fingers (one movable and a stationary on either side) forms two capacitors one between the movable finger and each stationary finger. The entire capacitance sensor is equivalent to two combined capacitances,  $C_1$  and  $C_2$ , as shown in Figure 7(a), namely,

$$C_1 = C_2 = C_0 = \epsilon N \frac{A}{d_0} (1 + f) \quad (4)$$

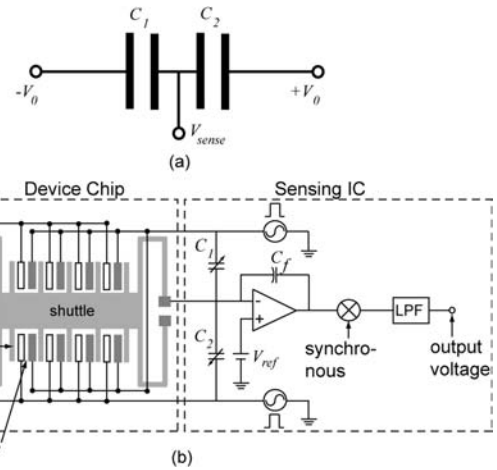


**Fig. 7.** (a) A simple model of the differential capacitor. (b) Double chip architecture used for measuring capacitance change. The capacitance change is proportional to the output voltage change.

where  $\epsilon$  is the electric permittivity,  $N$  is the number of unit movable fingers,  $A$  and  $d_0$  are the area of overlap and initial gap respectively between the movable finger and each stationary finger, and  $f = 0.65d_0/h$  is the fringing field correction factor with  $h$  being the beam height.<sup>48</sup>

The movable fingers are attached to the folded beams via the rigid movable shuttle so their displacements are equivalent. This displacement yields a change in capacitance given by,

$$\begin{aligned} \Delta C = C_1 - C_2 &= N\epsilon A \left( \frac{1}{d_0 - \Delta d} - \frac{1}{d_0 + \Delta d} \right) \\ &\approx \frac{2N\epsilon A}{d_0^2} \Delta d \end{aligned} \quad (5)$$

where  $\Delta d$  is the displacement of the load sensor. Note the fringing effect factor cancels. For displacements  $\Delta d$  with 50% of the initial gap  $d_0$ , the capacitance changes approximately linearly with the sensor displacement. This relatively large range of linear sensing is a major advantage of differential capacitance sensing over direct capacitance sensing which uses a single fixed beam for each movable beam.

A variety of circuit configurations may be used in measuring capacitance.<sup>34,35</sup> Figure 7 shows schematically the charge sensing method used in the device described in this paper. This method mitigates the effects of parasitic capacitances that generally occur in electrostatic MEMS devices. Here the change in output voltage  $\Delta V_{\text{sense}}$  is proportional to the capacitance change,<sup>25</sup>

$$\Delta V_{\text{sense}} = \frac{V_0}{C_f} \Delta C \quad (6)$$

where  $V_0$  is the amplitude of an AC voltage signal applied to the stationary fingers, and  $C_f$  the feedback capacitor as shown in Figure 6.

Minimizing stray capacitance and electromagnetic interference is critical in high resolution capacitance measurements. In this case, integrating the MEMS differential capacitor and sensing electronics on a single chip would minimize these effects, allowing detection of changes in capacitance at the atto-Farad level.<sup>35</sup> However this would greatly increase fabrication complexity. The double chip architecture depicted in Figure 7 is an alternative to the single chip scheme. Here the MEMS-based system is fabricated on one chip while a commercial integrated circuit chip (for example, Universal Capacitive Readout MS3110, Microsensors, Costa Mesa, CA) is used to measure changes in capacitance. Both chips are housed on a single printed circuit board.

### 2.3. System Analysis

With the mechanical response of the thermal actuator known for a given current input, it is now possible to formulate a set of equations governing the behavior of the entire device.<sup>24</sup> A lumped model of the entire device is constructed as shown in Figure 8. Here  $K_S$  is the stiffness of the tensile specimen,  $K_{LS}$  is the stiffness of the load sensor corresponding to the folding beams by which it is suspended,  $K_{TA}$  is the stiffness of the thermal actuator computed before, and  $U_{LS}$  is the displacement of the load sensor. The central shuttle is assumed to be rigid.

The governing equations for the lumped system shown in Figure 8 are given by:<sup>24</sup>

$$\begin{aligned} \Delta U_S &= U_{TA} - U_{LS} \\ U_{TA} &= \frac{2m\alpha\Delta TEAs - F_{TA}}{K_{TA}} \\ F_{TA} &= F_S = F_{LS} \\ F_S &= K_S\Delta U_S \\ F_{LS} &= K_{LS}U_{LS} \end{aligned} \tag{7}$$

where  $s = \sin \theta$  and  $\Delta U_S$  is the elongation of the specimen,  $E$  is the Young's modulus,  $\alpha$  is the coefficient of thermal expansion of the beam material, and  $m$  is the pairs of beams. Solving the system (Eq. (7)), the displacement of the thermal actuator  $U_{TA}$ , the tensile force on the specimen

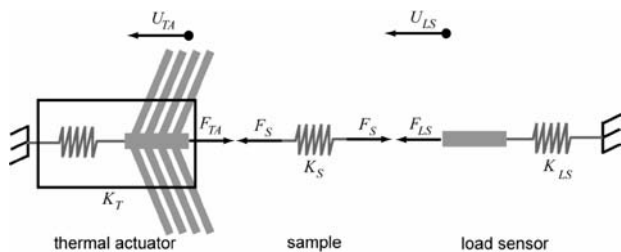


**Fig. 8.** Lumped model of the entire tensile loading device with internal forces and displacements shown in free body form.

$F_S$ , the elongation of the specimen  $\Delta U_S$ , and the corresponding displacement of the load sensor  $U_{LS}$  are obtained,

$$\begin{aligned} U_{TA} &= \frac{2m\alpha\Delta TEAs}{(K_{TA} + K_{TA}K_{LS}/K_S + K_{LS})} \\ &+ \frac{2m\alpha\Delta TEAs}{(K_{TA} + K_S + K_{TA}K_S/K_{LS})} \\ F_S &= \frac{2m\alpha\Delta TEAs}{(K_{TA}/K_S + 1 + K_{TA}/K_{LS})} \\ \Delta U_S &= \frac{2m\alpha\Delta TEAs}{(K_{TA} + K_S + K_{TA}K_S/K_{LS})} \\ U_{LS} &= \frac{2m\alpha\Delta TEAs}{(K_{TA} + K_{TA}K_{LS}/K_S + K_{LS})} \end{aligned} \tag{8}$$

where  $A$  is the cross-sectional area. These represent the critical parameters in obtaining force-displacement data using the MEMS-based tensile loading device.

Taking into consideration the above analyses, the following design criteria are set to achieve an effective and reliable material testing system:

- (1) Large load sensor displacements to maximize load resolution;
- (2) Low temperature at the actuator-specimen interface to avoid artificial heating of the specimen; and
- (3) The testing system operates as a displacement control i.e., the stiffness of the thermal actuator is significantly higher than that of the specimen and load sensor.

The specimen stiffness, failure load and elongation at failure ( $\Delta U_S$ ) dictate the choice of actuator geometry and the number and dimensions of the beams. Consequently optimization of the device design requires some preliminary knowledge of the specimen behavior as is customary in experimental mechanics.

## 3. EXPERIMENTAL RESULTS

### 3.1. Device Calibration

To calibrate the relationship between the measured capacitance and corresponding displacement, an otherwise identical device with a solid connection between the actuator and load sensor (i.e., no gap for specimen mounting) was fabricated on the same chip. Real time high resolution images were employed to calibrate the capacitance measurements<sup>25</sup> within a field emission SEM (Leo Gemini 1525). The device was actuated with a series of stepwise increasing voltages, applied sequentially in six ON-OFF cycles. A high contrast feature on the movable shuttle was selected for capturing images at high magnification ( $\times 183$  k). The device state during successive ON-OFF actuation cycles was captured in a single SEM image, as shown in Figure 9(a). Simultaneously, the output voltage  $V_{sense}$  was recorded by a digital multimeter and converted to capacitance change using (Eq. (6)). Figure 9(b) shows the raw data of  $V_{sense}$  at an actuation voltage of 5.5 V.

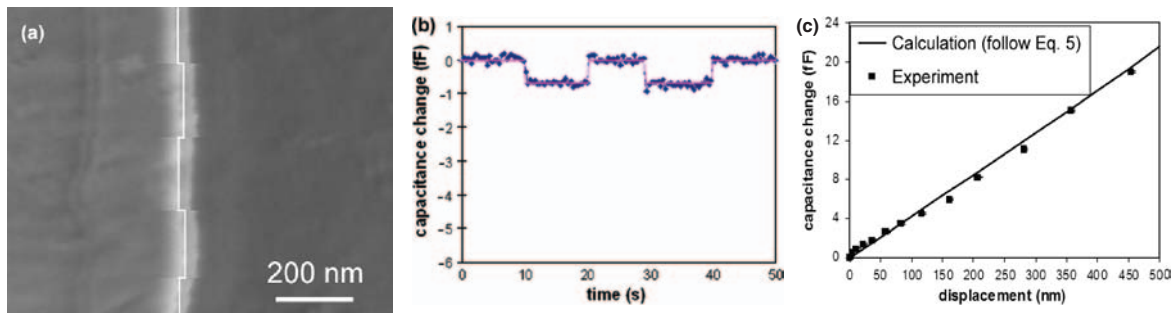


**Fig. 9.** Calibration of the load sensor showing the relationship between capacitance change and measured displacement from SEM images at a series of actuation voltage. (a and b) Signatures when actuator is at 2 V; reference feature in the SEM image showing a motion of 15 nm due to four ON–OFF actuations (a), and plot corresponding to a 0.7 fF capacitance change resulting from the same actuation (b). Both raw data and fitted data are shown in the plot of capacitance measurements. (c) Plot of displacement versus capacitance change resulting from the calibration.

The images were analyzed to identify displacements with the following procedure: the line-by-line scanning was transformed to an intensity matrix of  $1024 \times 768$  pixels. To correlate the OFF to ON images, two polynomial functions were used to fit the intensity distribution for the last scanned line corresponding to OFF,  $f(x)$ , and for the first scanned line corresponding to ON,  $g(x)$ , respectively. These two functions were interpolated to a sub-pixel level and the shift,  $u$ , was obtained by finding the best match between functions  $f(x)$  and  $g(x+u)$ . The iterative process was stopped when  $\int_{\Omega} [g(x+u) - f(x)]^2 dx$  was smaller than a prescribed tolerance. The domain  $\Omega$  was defined to span the feature in the movable shuttle. Using the calibration factor of the SEM image at the corresponding scale, we converted the shift  $u$  in pixels to displacement (nm). Note that this image analysis has the advantage of eliminating the influence of drift, which typically accumulates with time, and provides sub-pixel resolution.

Figure 9(c) shows a series of experimental data correlating the displacements/loads and the capacitance changes (in dots). The relationship between displacement and capacitance change as predicted in Eq. (5) is plotted in solid line.<sup>26</sup> It is evident that the experimental data agree with the prediction very well. The achievable resolution of the measured capacitance change is 0.2 fF, and the corresponding displacement resolution is 3 nm.

Another important step in the calibration procedure is the accurate measurement of the load sensor stiffness. This can be accomplished in one of two ways: (i) by resonating the structure, a common procedure in MEMS research,<sup>25</sup> or (ii) by identifying the Young's modulus of the material,  $E$ , and then using finite element analysis (FEA) with accurate metrology to determine the structural stiffness. For the parallel beams in the load sensor, the resonating voltage is larger than the *pull-in* voltage so the second methodology was employed. Since the load sensor and actuator are comprised of the same material, the accuracy of the load sensor stiffness prediction was assessed by determining the comb-drive actuator stiffness using the resonance method and then comparing this result with the one calculated by FEA. In the resonance method, the stiffness is calculated

by  $K = (2\pi f_r)^2 (M_s + 0.3714M_b)$ ,<sup>25</sup> where  $f_r$  is the resonant frequency,  $M_s$  and  $M_b$  the masses of the shuttle and the folded beams, respectively. For the comb-drive actuator, we measured a resonant frequency of  $17.2 \pm 0.1$  kHz. The corresponding stiffness is 20.3 N/m, while the computed stiffness based on the *measured* folded beam geometry, using  $E = 170$  GPa,<sup>17</sup> was 20.7 N/m. This clearly shows that the stiffness computed based on the fabricated geometry and the known value of Young's modulus is in good agreement with that identified from the resonance experiment. Following this procedure, the stiffness of the load sensor designed for the testing CNTs was computed to be 11.8 N/m, which corresponds to a load resolution of 35 nN.<sup>25</sup> Likewise, the stiffness of the load sensor designed for testing NWs was 48.5 N/m with a load resolution of 145 nN.

### 3.2. Tensile Tests of Polysilicon Thin Films

The size and fragile nature of nano-scale materials and structures demands specialized techniques for preparation and mounting on the MEMS device. Thin films may be cofabricated with the MEMS device. This eliminates any handling. For example, freestanding polysilicon films were cofabricated with the MEMS device between the actuator and the load sensor (Fig. 10(a)).<sup>23</sup> Due to limitations in the resolution of the photolithography used to make the devices, the initial specimen width could not be made thinner than approximately  $2 \mu\text{m}$ . To reduce this dimension, the polysilicon specimen was further machined by focused ion beam (FIB) down to 350–450 nm.

Thin film specimens cofabricated with the MEMS device were then tested in the SEM. The results of a tensile test of a polysilicon specimen prepared as described above are shown in Figure 10(b). Here the stress–strain curve shows strong linearity with a Young's modulus of  $156 \pm 17$  GPa.<sup>24</sup> This result is consistent with other reported values for polysilicon films.<sup>10, 11, 49</sup>

### 3.3. Tensile Tests of Nanowires

It is known that nanowires possess a relatively large surface area-to-volume ratio. Consequently interfaces, interfacial

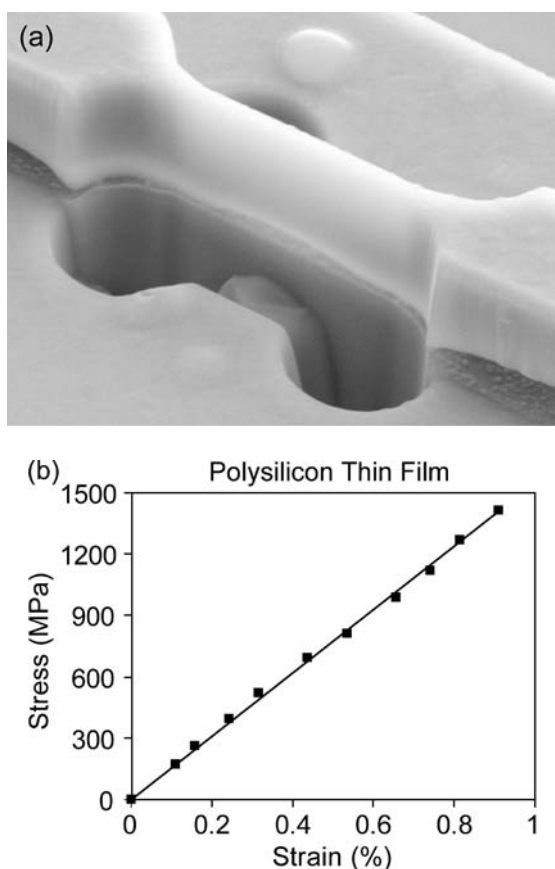


**Fig. 10.** (a) A polysilicon thin film tensile specimen cofabricated with the MEMS device and further thinned by FIB machining. (b) Stress-strain data for a polysilicon thin film specimen. Reprinted with permission from [24], Y. Zhu et al., *J. Micromechanics Microengineering* 16, 242 (2006). © 2006.

energy and surface topography play an increasingly important role in their deformation and failure processes. In larger structures, generation and propagation of defects dictates material behavior. As grain sizes or structural dimensions fall below 50 to 100 nm, surface and intermolecular mechanisms gain influence over material behavior. Therefore understanding the mechanics of these new materials and structures is essential. As an example, zinc oxide (ZnO) nanowires are studied.

Individual nanowires and nanotubes may either be grown across the gap between the actuator and load sensor or placed by nanomanipulation.<sup>23</sup> This procedure involves use of a nanomanipulator operated within an SEM to pick up and place an individual nanostructure across the gap, followed by electron beam-induced deposition (EBID) of platinum to weld the ends of the structure in place.

*In situ* SEM tensile tests of ZnO nanowires (obtained from NanoLab Inc.) using the MEMS device allow us to record the material stress-strain behavior and failure. Figure 11(a) shows sequential SEM images of the *in situ* SEM tensile testing. The nanowire specimen began to deform at an actuation voltage of 0.8 V and failed at 8.5 V.

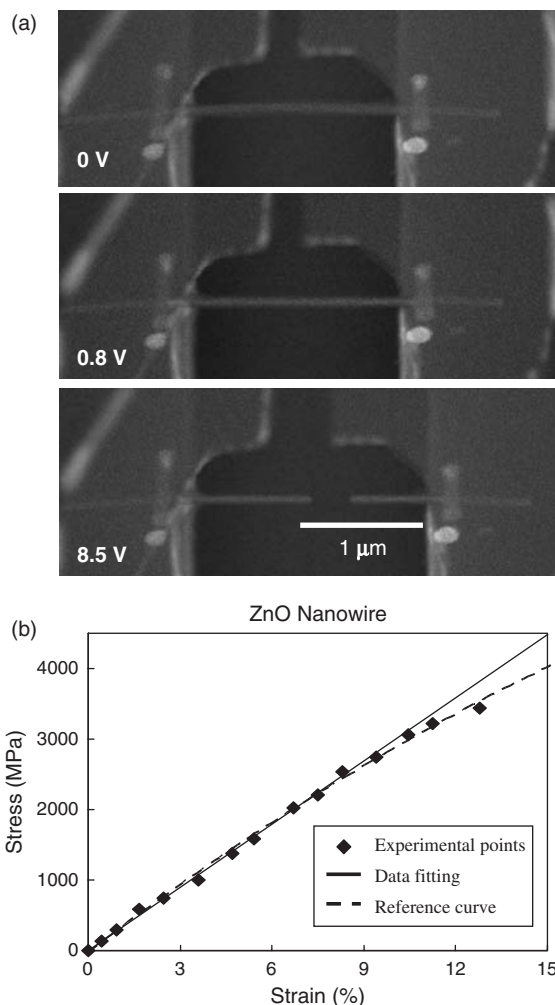


**Fig. 11.** *In situ* SEM tensile testing of a ZnO nanowire. (a) Sequential SEM images of a tensile loading process. The nanowire is 2.2  $\mu\text{m}$  in length and 90 nm in width. (b) The strain-stress data.

The strain-stress data, shown in Figure 11(b), reveals an interesting point. The nanowire was stressed to 3.5 GPa, value this significantly higher than the yield stress of bulk ZnO,<sup>50,51</sup> and remained elastic to a strain of about 10%. The failure strain exceeded 12%, a very large strain for a brittle material. This phenomenon, which is attributed to the absence of defects and high stress threshold for the nucleation of defects,<sup>16,52</sup> confirms that the strength of the material increases as the specimen characteristic dimension decreases. Ultimately, the strength is expected to approach the theoretical strength of the material (approximately 1/10 of its Young's modulus).<sup>50</sup> In this case, a modulus of 30 GPa was measured. Hence, the measured failure stress indeed reached the theoretical strength.

### 3.4. Tensile Test of Carbon Nanotubes and the Effects of Irradiation

*In situ* SEM and TEM tensile tests of MWNTs using the MEMS device allow insight into their failure mechanism.

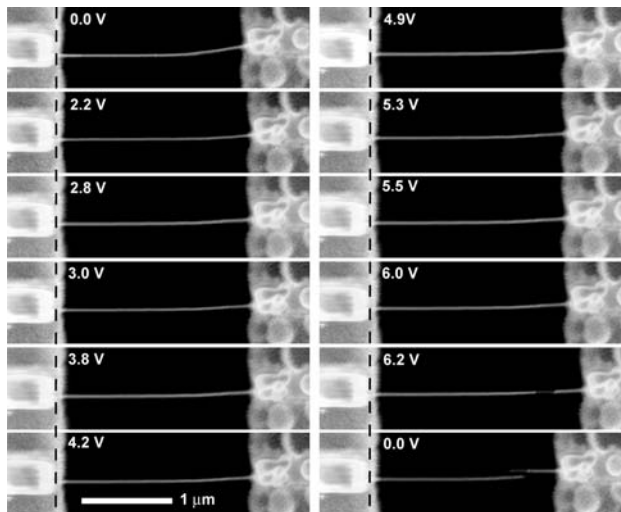


**Fig. 12.** Sequential SEM images of a multi-walled carbon nanotube subjected to tension. The nanotube is 2  $\mu\text{m}$  in length and 42 nm in diameter. Failure occurs at an actuation voltage of 6.2 V corresponding to a load of 2177 nN and a stress of 48.5 GPa.

Figure 12 shows sequential images of the tensile loading of a MWNT *in situ* a SEM. The specimen was mounted in the MEMS device minimizing electron radiation. The relevance of this feature will become apparent when the results from *in situ* TEM are discussed next.

Fracture occurs in a typical “sword-in-sheath” fashion,<sup>12</sup> with presumable the outermost shell breaking and subsequent inner concentric shells telescoping out. The two ends of the outermost shell are clamped to the testing device using EBID of platinum.<sup>23</sup> Consequently, it is likely that the outermost shell carries the load and breaks under tensile loading as only van der Waals interactions between the concentric inner shells are expected. Based on the assumption that there is minimal load transfer between the outermost shell and subsequent inner shells, stress and strain are often calculated using the measured outer diameter of the MWNT and an assumed shell thickness of 0.34 nm (equal to the interlayer distance of 0.34 nm),<sup>13,53</sup> as opposed to using the combined thickness of all the concentric shells. The computed values are reported in Table I as test number 6. The measure load-displacement behavior is shown

in Figure 13. A Young modulus of 1 TPa was measured under the assumption of outermost shell failure.

In contrast to tests of unmodified MWNTs, tensile tests of MWNTs exposed to high-energy electron or ion beam irradiation reveal that multiple shells or the entire cross section break simultaneously, resulting in greater stiffness.<sup>54</sup> This observation suggests that the irradiation introduces cross links between shells, resulting in load transfer. A series of tests demonstrating this effect were performed using the MEMS device on MWNTs exposed to varying degrees of ion or electron beam radiation, as well as on unexposed MWNTs as a control.<sup>26</sup> These tests are reported in Figure 13 and Table I. Here it is important to note that the irradiation energy of the electron beam used for SEM imaging during mounting of the MWNTs on the MEMS device is well below the threshold for atomic structure modification and thus is assumed to have negligible effects relative to the high-energy electron (TEM) and ion beam exposure (FIB).

MWNTs exposed to ion irradiation demonstrated significantly greater stiffness than those that were not. In Test 1 (see Table I), the MWNT was irradiated with Ga<sup>+</sup> ions at a flux of  $10^{13}$  e  $\text{cm}^{-2}$  s<sup>-1</sup> for 10 seconds using a 30 kV accelerating voltage. An *in-situ* TEM tensile test was then performed using the MEMS device. The corresponding inset of Figure 13 shows clearly that the entire cross section breaks as opposed to the typical telescoping, “sword-in-sheath” mechanism. Thus stress and modulus values reported in Table I, which were computed assuming only the outermost shell to be load bearing, appear meaningless in this case. In fact, ion irradiated specimens exhibit values of Young’s modulus of 5,200 and 4,000 GPa which are significantly higher than those reported elsewhere in the literature.<sup>12, 13, 53</sup> For example, Ding et al. report moduli ranging from 620 to 1,200 GPa based on the assumption that only the outermost shell is load bearing. However, *in situ* SEM does not provide evidence that only the outer wall breaks.

MWNTs exposed to electron beam irradiation also showed greater stiffness than the unexposed sample, although to a lesser degree. In Test 4 (see Table I), the MWNT was exposed to electron beam radiation with a flux

**Table I.** Irradiation conditions and measured mechanical properties of six MWNTs. Shown are the case number, gauge length, outer diameter, applied force at fracture, elongation, tensile strength<sup>a</sup> and Young’s modulus<sup>a</sup>.

Test #	Gauge length [ $\mu\text{m}$ ]	Outer diameter [nm]	Ion radiation dose [ $\text{e cm}^{-2}$ ]	Electron radiation dose [ $\text{e cm}^{-2}$ ]	Breaking force [ $\mu\text{N}$ ]	$\Delta L$ [nm]	$\sigma_s^a$ [Gpa]	$E^a$ [Gpa]
1	6.69	191	$10^{14}$	—	31.1	195.6	152.5	5,200
2	3.02	142	$0.5 \times 10^{14}$	—	20.4	101.2	134.5	4,000
3	2.85	169	—	$4.5 \times 10^{21}$	9.9	143.8	54.8	1,100
4	3.3	108	—	$1.5 \times 10^{21}$	4.3	97.5	37.3	1,300
5	3.82	96	—	—	1.9	221.9	18.5	300
6	2.06	42	—	—	2.2	96.8	48.5	1,000

<sup>a</sup>Stress is computed under the assumption that only the outermost shell of the MWNT bears the load (i.e., the cross-sectional area is taken to be that of the outermost shell alone).

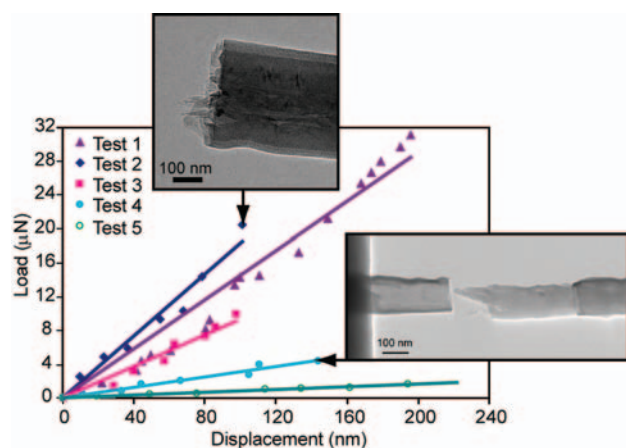


**Fig. 13.** Force-displacement data measured for multi-walled carbon nanotubes exposed to varying degrees and types of radiation. Corresponding irradiation conditions and test parameters are summarized in Table I.

of  $1.5 \times 10^{19} \text{ e cm}^{-2} \text{ s}^{-1}$  for 100 seconds within the TEM at an acceleration voltage of 200 kV. In this case, the failure was telescopic in nature as shown in the corresponding inset of Figure 13. However, high-resolution TEM images show that more than one shell broke rather than only the outermost shell. Thus again, the reported values of stress and strain do not accurately represent the true parameters of the material.

Tensile tests of MWNTs exposed to high-energy electron or ion beam irradiation reveal changes in the mode of failure,<sup>26</sup> suggesting that the irradiation introduces cross links between shells. Other reports provide corroborating evidence through experiments and first principle calculations. Above a certain energy threshold, electron and ion beams can produce vacancies in the nanotube shells and corresponding interstitials in the inter-shell spacing.<sup>26</sup> Moreover molecular dynamics simulations revealed that these interstitial atoms can form stable and covalent bonds between shells.<sup>56</sup> These simulations further demonstrated that the development of covalent bonds under moderate beam irradiation can increase the failure strength of MWNTs while excessive irradiation degrades the mechanical properties due to structural damage (cluster of vacancies) and/or amorphization.<sup>55,56</sup> The experimental observations reported here agree strongly with the predictions of these simulations.

These findings suggest that both electron and ion irradiation could be used to enhance the mechanical properties of MWNTs. Moreover and in light of the observed changes in failure mechanisms, conclusions based on stress and strain data computed under the assumption that only the outermost shell bears the load should be drawn with caution. The observations reported here suggest there is some degree of load sharing between shells. For this reason, the data reported here focus on the stiffness of the nanostructures which were measured directly. With advances in TEM image acquisition, the MEMS-based testing technique reported here should allow direct imaging of the evolution

of the failure and determination of the number of shells failing simultaneously.

#### 4. SUMMARY

Mechanical characterization of nanometer-scale materials and structures presents a unique set of challenges. The excellent force and displacement resolution of MEMS make them ideal systems to meet these challenges. This letter presented the modeling and analysis involved in the design of a MEMS-based material testing system allowing simultaneous load-displacement measurement combined with *real-time high resolution* SEM or TEM imaging of the specimen. This system uses a thermal actuator to apply a tensile load and a differential capacitance displacement sensor of known stiffness to electronically measure the applied load. An analytical model of the thermal actuator involved an electrothermal analysis, to determine the temperature distribution in the actuator, followed by a thermomechanical analysis to determine the resulting displacement. A coupled-field finite element analysis was employed to verify the analytical model and obtain further insight on the field variables. The differential capacitive load sensor was analyzed to determine the output voltage for a given displacement. A set of design criteria was established based on the analyses as guidelines for the design of similar devices. Finally examples of application of the MEMS-based material testing system to cofabricated polysilicon thin films, ZnO nanowires, and multi-walled carbon nanotubes were presented. The tests performed on ZnO nanowires demonstrated increased strength approaching the material theoretical strength. Tensile tests of multi-walled carbon nanotubes exposed to varying degrees of electron and ion beam irradiation showed differences in failure mechanisms and an increase in stiffness with the level of irradiation. This is attributed to the formation of cross links between shells.

**Acknowledgments:** The authors thank Alberto Corigliano for valuable contributions in the modeling of the thermal actuator, E. Olson and J.-G. Wen for their contribution in the development of the *in-situ* TEM holder, C. Li for assistance in the *in-situ* TEM experiments and O. Loh for helpful discussions during the preparation of this manuscript. This work was supported by National Science Foundation Grant DMR-0315561. Nanomanipulation was carried out in the Center for Micro-analysis of Materials at the University of Illinois, which is partly supported by the U.S. Department of Energy under Grant DEFG0296-ER45439.

#### References and Notes

1. M. M. J. Treacy, T. W. Ebbesen, and J. M. Gibson, *Nature* 381, 678 (1996).
2. P. Poncharal, Z. L. Wang, D. Ugarte, and W. A. de Heer, *Science* 283, 1513 (1999).

3. P. E. Marszalek, W. J. Greenleaf, H. Li, A. F. Oberhauser, and J. M. Fernandez, *PNAS* 97, 6282 (2000).
4. W. C. Oliver and G. M. Pharr, *J. Mater. Res.* 7, 1564 (1992).
5. M. T. A. Saif and N. C. MacDonald, *Sens. Actuators A* 52, 65 (1996).
6. H. Kahn, R. Ballarini, R. L. Mullen, and A. H. Heuer, *Proc. Royal Society of London A* 455, 3807 (1999).
7. E. Wong, P. Sheehan, and C. Lieber, *Science* 277, 1971 (1997).
8. D. A. Walters, L. M. Ericson, M. J. Casavant, J. Liu, D. T. Colbert, K. A. Smith, and R. E. Smalley, *Appl. Phys. Lett.* 74, 3803 (1999).
9. J. P. Salvetat, G. A. D. Briggs, J. M. Bonard, R. R. Bacsá, A. J. Kulik, T. Stockli, N. A. Burnham, and L. Forro, *Phys. Rev. Lett.* 82, 944 (1999).
10. I. Chasiotis and W. G. Knauss, *J. Mech. Phys. Solids* 51, 1533 (2003).
11. W. N. Sharpe, K. M. Jackson, and K. J. Hemker, *J. MEMS* 10, 317 (2001).
12. M.-F. Yu, O. Lourie, M. J. Dyer, K. Moloni, T. F. Kelly, and R. S. Ruoff, *Science* 287, 637 (2000).
13. W. Ding, L. Calabri, K. Kohlhaas, X. Chen, D. Dikin, and R. Ruoff, *Experimental Mechanics* 47, 25 (2006).
14. Z. W. Pan, S. S. Xie, L. Lu, B. H. Chang, L. F. Sun, W. Y. Zhou, G. Wang, and D. L. Zhang, *Appl. Phys. Lett.* 74, 3152 (1999).
15. H. D. Espinosa, B. C. Prorok, and M. Fischer, *J. Mech. Phys. Solids* 51, 47 (2003).
16. H. D. Espinosa, B. Prorok, and B. Peng, *J. Mech. Phys. Solids* 52, 667 (2004).
17. H. D. Espinosa, B. Peng, B. C. Prorok, N. Moldovan, O. Auciello, J. A. Carlisle, D. M. Gruen, and D. C. Mancini, *J. Appl. Phys.* 94, 6076 (2003).
18. H. D. Espinosa and B. Peng, *J. MEMS* 14, 153 (2005).
19. A. Haque and M. T. A. Saif, *Experimental Mechanics* 42, 123 (2002).
20. A. Haque and M. T. A. Saif, *PNAS* 101, 6335 (2004).
21. R. C. Hugo, H. Kung, J. Weertman, R. Mitra, J. Knapp, and D. Follstaedt, *Acta Mater.* 51, 1937 (2003).
22. M. Ke, S. A. Hackney, W. W. Milligan, and E. C. Aifantis, *Nanostruct. Mater.* 5, 689 (1995).
23. Y. Zhu and H. D. Espinosa, *PNAS* 102, 14503 (2005).
24. Y. Zhu, A. Corigliano, and H. D. Espinosa, *J. Micromechanics Microengineering* 16, 242 (2006).
25. Y. Zhu, N. Moldovan, and H. D. Espinosa, *Appl. Phys. Lett.* 86, 242 (2005).
26. H. D. Espinosa, Y. Zhu, and N. Moldovan, *J. MEMS* (2007). (To appear)
27. W. van Arsdell and S. Brown, *J. MEMS* 8, 319 (1999).
28. H. Kahn, N. Tayebi, B. Ballerini, R. Mullen, and A. Heuer, *Sens. Actuators A* 82, 274 (2000).
29. H. Kahn, B. Ballerini, and A. Heuer, *MRS Bull.* 26, 300 (2001).
30. L. Chu, L. Que, and Y. Gianchandani, *J. MEMS* 11, 489 (2002).
31. E. Fischer and P. Labossiere, *Proceedings of the SEM Annual Conference on Exp. and Appl. Mechanics*, Milwaukee, WI (2002).
32. W. C. Tang, T. C. H. Nguyen, and R. T. Howe, *Sens. Actuators A* 20, 25 (1989).
33. R. Legtenberg, A. W. Groeneveld, and M. Elwenspoek, *J. Micromechanics Microengineering* 6, 320 (1996).
34. S. D. Senturia, *Microsystem Design*, Kluwer Academic Publishers, Boston (2002).
35. P. E. Boser, *Electronics for micromachined inertial sensors*, *Proc. Transducers*, Chicago, IL (1997).
36. M. Zhang, E. A. Olson, R. D. Twesten, J. G. Wen, L. H. Allen, I. M. Robertson, and I. Petrov, *J. Mater. Res.* 20, 1802 (2005).
37. A. A. Geisberger, N. Sarkar, M. Ellis, and G. D. Skidmore, *J. MEMS* 12, 513 (2003).
38. J. S. Park, L. L. Chu, A. D. Oliver, and Y. B. Gianchandani, *J. MEMS* 10, 247 (2001).
39. L. L. Chu and Y. B. Gianchandani, *J. Micromechanics Microengineering* 13, 279 (2003).
40. M. F. Pai and N. C. Tien, *Sens. Actuators A* 83, 237 (2000).
41. H. Kapels, R. Aigner, and J. Binder, *IEEE Transactions on Electron Devices* 47, 1522 (2000).
42. M. Chiao and L. W. Lin, *J. MEMS* 9, 146 (2000).
43. C. D. Lott, T. W. Mclain, J. N. Harb, and L. L. Howell, *Sens. Actuators A* 101, 239 (2002).
44. Q. A. Huang and N. K. S. Lee, *Microsystem Technologies-Micro-and Nanosystems-Information Storage and Processing Systems* 5, 133 (1999).
45. N. D. Mankame and G. K. Ananthasuresh, *J. Micromechanics Microengineering* 11, 452 (2001).
46. L. Que, J. S. Park, and Y. B. Gianchandani, *J. MEMS* 10, 247 (2001).
47. B. E. Boser and R. T. Howe, *IEEE Journal of Solid-State Circuits* 31, 366 (1996).
48. J. M. Huang, K. M. Liew, C. H. Wong, S. Rajendran, M. J. Tan, and A. Q. Liu, *Sens. Actuators A* 93, 273 (2001).
49. A. Corigliano, B. De Masi, A. Frangi, C. Comi, A. Villa, and M. Marchi, *J. MEMS* 13, 200 (2004).
50. T. H. Courtney, *Mechanical Behavior of Materials*, McGraw-Hill (2000).
51. A. V. Desai and M. A. Haque, *Sens. Actuators A* 134, 169 (2007).
52. A. J. Kulkarni, M. Zhou, and F. J. Ke, *Nanotechnology* 16, 2749 (2005).
53. A. Barber, I. Kaplan-Ashiri, S. Cohen, R. Tenne, and H. Wagner, *Compos. Sci. Technol.* 65, 2830 (2005).
54. W. Smith and D. Luzzi, *J. Appl. Phys.* 90, 3509 (2001).
55. M. Huhtala, A. Krashennnikov, J. Aittoniemi, S. Stuart, K. Nordlund, and K. Kaski, *Phys. Rev. B* 79, 045404 (2004).
56. J. Pomoell, A. Krashennnikov, K. Nordlund, and J. Keinonen, *J. Appl. Phys.* 96, 2864 (2004).